

Removing Interlopers From Intensity Mapping Probes Of Primordial Non-Gaussianity

Chang Chen,^{1*} Anthony R. Pullen,^{1,2}

¹Center for Cosmology and Particle Physics, Department of Physics, New York University, 726 Broadway, New York, NY, 10003, U.S.A.

²Center for Computational Astrophysics, Flatiron institute, New York, NY 10010, U.S.A.

Accepted XXX. Received YYY; in original form ZZZ

ABSTRACT

Line intensity mapping (LIM) has the potential to produce highly precise measurements of scale-dependence bias from primordial non-Gaussianity (PNG) due to its ability to map much larger volumes than are available from galaxy surveys. PNG parameterized by f_{NL} leads to a scale-dependent correction to the bias, and therefore a correction to the line intensity power spectrum. However, LIM experiences contamination from foreground emission, including interloping emission lines from other redshifts which alter the power spectra of the maps at these scales, potentially biasing measurements of f_{NL} . Here we model the effect of line interlopers on upcoming line intensity mapping probes of primordial non-Gaussianity (PNG) from inflation. As an example, we consider the [CII] line at target redshift $z_t = 3.6$ to probe PNG, with the important systematic concern being foreground contamination from CO lines residing at redshifts different from the target redshift. We find interloper lines can lead to a significant bias and an increase in errors for our PNG constraints, leading to a false positive for non-standard inflation models. We model how well the cross-correlation technique could reduce this interloper contamination. We find the uncertainty of f_{NL} reduces by factors of two and six for local and orthogonal shape PNG respectively, and by a factor of five for local shape if we consider seven interloper lines, almost eliminating the effect of interlopers. This work shows that using cross-power and auto-power spectra of line intensity maps jointly could potentially remove the effects of interlopers when measuring non-Gaussianity.

Key words: large-scale structure of Universe – diffuse radiation – inflation

1 INTRODUCTION

Inflation theory has been enormously successful in explaining the origin of large-scale structure in the universe (Guth 1981; Linde 1987). The simplest inflation model predicts almost scale-invariant, adiabatic and Gaussian perturbations. Primordial Non-Gaussianity (PNG) of the local shape is parameterized by f_{NL}^{loc} (Komatsu & Spergel 2001; Gangui et al. 1994) as

$$\Phi = \phi + f_{NL}^{loc} \phi^2 \quad (1)$$

where ϕ is the Gaussian primordial potential. The parameter f_{NL} for the standard single-field inflation model is very small, of order 10^{-2} (Maldacena 2003), while f_{NL}^{loc} for more general models, e.g. multi-field inflation (Linde & Mukhanov 1997; Lyth et al. 2003) is much higher, even up to $f_{NL} \sim O(1)$. In addition, the orthogonal shape PNG, which can be produced by models with higher derivative interactions and Galilean inflation (Senatore et al. 2010), is parameterized by f_{NL}^{orth} . Therefore, probing f_{NL} can serve as a strong discriminant among cosmological models.

Currently, the best constraints on f_{NL} are from CMB bispectra

measurements from Planck satellite, given as $f_{NL}^{loc} = -0.9 \pm 5.1$ and $f_{NL}^{orth} = -38 \pm 24$ (Planck Collaboration et al. 2019). Complementary large-scale structure (LSS) surveys such as BOSS (Alam et al. 2017), DES (Abbott et al. 2018), EUCLID (Amendola et al. 2018) could probe f_{NL} scale-dependent bias on large scales (Matarrese & Verde 2008; Afshordi & Tolley 2008) and are promising to achieve higher precision than CMB data. As of now, current constraints on f_{NL}^{loc} from scale-dependent bias are not yet competitive with CMB constraints (Leistedt et al. 2014; Castorina et al. 2019; Dai & Xia 2020), with the most precise constraints still coming from quasars in Leistedt et al. (2014), $-49 < f_{NL}^{loc} < 31$. For PNG of the general shape, non-zero primordial bispectrum induces a scale-dependent correction to the bias (Dalal et al. 2008; Matarrese & Verde 2008; Afshordi & Tolley 2008; Desjacques et al. 2011), leaving a signature in the power spectrum on large scales.

Unlike galaxy surveys which probe individual tracers, line intensity mapping measures cumulative intensity fluctuations from all luminous sources including faint ones unresolved in galaxy surveys. Line intensity mapping experiments could have the potential to access over 80% of the volume of the observable Universe (Kovetz et al. 2019). Therefore, it has the potential to further the study of large-scale structure in the universe, especially of the Epoch

* E-mail: changchen@nyu.edu

of Reionization when sources with low luminosity inaccessible to galaxy surveys reionized the universe (Robertson et al. 2015). The fine-structure line from ionized carbon ([CII]) (Gong et al. 2012; Silva et al. 2015), the brightest line for star formation galaxies, makes it an ideal candidate for probing the line intensity power spectrum on large scales to improve constraints of PNG (Moradinezhad Dizgah & Keating 2019; Moradinezhad Dizgah et al. 2019).

An important systematic effect when considering intensity mapping is foreground interloper emission (Visbal & Loeb 2010; Lidz & Taylor 2016) from lines residing at the same *observed* frequency as the target line. Interloper emission, in which different emission lines from galaxies with different epochs redshift to the same observed frequency, contaminates intensity maps and introduces extra correlations in the measured power spectrum that can bias parameter estimations. This deposits a distinct signature at large scales where effects from non-Gaussianity reside due to the features in the power spectrum at these scales such as baryon acoustic oscillations and the peak corresponding to matter-radiation equality.

In our case, we consider a target line of [CII] emission with rest-frame frequency $\nu_t = 1901$ GHz emitted from sources at redshift z_t contaminated by interloping rotational lines of carbon monoxide (CO ($J \rightarrow J - 1$)) (Visbal & Loeb 2010) with rest-frame frequency $\nu_i = 115 \times JGHz$ emitted from sources at redshifts z_i lower than target redshift z_t . Those CO lines can be confused as [CII] line if they reside at the same observed frequency ν_{obs} as the target line, i.e. $\nu_{obs} = \nu_t/(1 + z_t) = \nu_i/(1 + z_i)$. These interloper CO lines can distort power spectrum detections and contaminate the forecast for constraints on PNG. A recent paper (Gong et al. 2020) discusses the interloper contamination on constraints of cosmological and astrophysical parameters. Assuming the target redshift z_t in converting the observed frequencies and angles to their co-moving coordinates, the interloper lines will be mapped to the wrong longitudinal and transverse co-moving wavenumbers, causing an anisotropy of the interloper power spectrum contribution (Visbal & Loeb 2010; Gong et al. 2014; Lidz & Taylor 2016).

In this paper we adopt this approach, where we seek how best to reduce the contamination when measuring f_{NL} using power spectrum measurements. In this work we consider a line intensity mapping survey using a Planck-like telescope with a high-resolution spectrograph, similar to the instrument modeled in Moradinezhad Dizgah et al. (2019), to forecast measurement errors for f_{NL} . We find through a Fisher analysis that not only do interlopers significantly increase the error on f_{NL} , but that a properly modeled auto-power spectrum analysis cannot reduce the error effectively. Specifically, we find that interlopers can bias the f_{NL} measurement, producing a false 3σ detection of non-Gaussianity favoring non-standard inflation models.

Next, we consider cross-correlation to separate anisotropic interloper emission from the [CII] auto power spectrum. We model the cross-correlation between [CII] and CO(4-3) at the same redshift, $z = 3.6$ in our case with a different frequency to avoid bias from interloper emission. We calculate auto-power spectra and cross-power spectrum of [CII] and CO(4-3) maps and perform a Fisher analysis to forecast the errors. We find the interloper contamination for the PNG probing can be largely removed using this method, reducing the Fisher analysis error by factors of two and five for f_{NL}^{loc} and f_{NL}^{orth} respectively if we only consider 1 interloper line, and by a factor of five for f_{NL}^{loc} if we consider 7 interloper lines. For both cases we find that including the cross-power in the analysis removes most of this interloper bias, making the f_{NL} measurement rather insensitive to contamination from interlopers. However, we also find

that the auto-power spectra can still play a large role in regards to the precision of the f_{NL} measurement. Specifically, we find that for f_{NL}^{loc} , the precision comes solely from the cross-power spectrum, while for f_{NL}^{orth} the precision comes roughly equally from the auto-power and cross-power spectra.

The outline of the rest of the paper is as follows. In Section 2, we review the theoretical model of the line intensity power spectrum detection for PNG, and the interloper contamination for this detection. In Section 3, we describe the Fisher analysis and data bias approach. In Section 4, we detail our fiducial survey and present the results for constraints on f_{NL}^{loc} . We further discuss the prospect for using cross-correlation with another emission line in Section 5. In Section 6 we forecast the constraints on the orthogonal shape PNG. We further consider different astrophysical models in Section 7. Based on our results, we draw our conclusions in Section 8. Throughout this paper we adopt a flat cosmological model with $H_0 = 67.74$, $\Omega_m = 0.26$, $\Omega_b = 0.049$, $\sigma_8 = 0.816$.

2 PNG LINE INTENSITY POWER SPECTRUM DETECTION AND INTERLOPER CONTAMINATION

In this section we review the formalism for the scale-dependent correction to clustering bias due to non-zero f_{NL} , present how this correction to bias would manifest itself in the line intensity power spectrum detection, and highlight the interloper contamination of the power spectrum.

2.1 PNG review

Local shape PNG is produced by super-horizon non-linear evolution of primordial curvature perturbations. In the absence of PNG, on large scales the halo bias b_h is assumed to be constant. Local shape PNG, parameterized by f_{NL}^{loc} , leads to a scale-dependent correction to the linear halo bias (Dalal et al. 2008; Matarrese & Verde 2008; Afshordi & Tolley 2008).

$$b_h(M, z) \rightarrow b_h(M, z) + \Delta b_h^{loc}(M, k, z) \quad (2)$$

$$\Delta b_h^{loc}(M, k, z) = \frac{3f_{NL}^{loc} \delta_c [b_h(M, z) - 1] \Omega_m H_0^2}{k^2 T(k) D(z)} \quad (3)$$

where $\delta_c = 1.686$ is the threshold of spherical collapse at $z = 0$, $T(k)$ is the matter linear transfer function $T(k \rightarrow 0) = 1$ and $D(z)$ is the normalized linear growth factor [$D(z = 0) = 1$].

On large scales this k^{-2} scale-dependent correction has been used to constrain f_{NL}^{loc} from power spectrum detections of LSS biased tracers due to its clean signal (Slosar et al. 2008; Leistedt et al. 2014; Ho et al. 2015). Alternatively, line intensity mapping can provide a more economical survey over larger volume to probe power spectrum on large scales.

Orthogonal shape PNG can be produced by models with higher-derivative interactions and Galilean inflation (Senatore et al. 2010). Parameterized by f_{NL}^{orth} , on large scales, orthogonal shape PNG leads to a scale-dependent correction to the linear halo bias (Desjacques et al. 2011)

$$\Delta b_h^{orth}(k) = -6f_{NL} \frac{\sigma_{as}^2}{\sigma_{0s}^2} \left[(b_h - 1)\delta_c + 2 \left(\frac{\partial \ln \sigma_{as}}{\partial \ln \sigma_{0s}} - 1 \right) \right] \times k^{-2\alpha} \mathcal{M}_{R_s}(k, z)^{-1} \quad (4)$$

$\alpha = (n_s - 4)/6$, $\mathcal{M}_{R_s}(k, z) = W_{R_s}(k) \mathcal{M}(k, z)$, where $\mathcal{M}(k, z) =$

$\frac{2}{5} \frac{k^2 T(k) D(z)}{\Omega_m H_0^2}$, and we choose the window function $W_{R_s}(k)$ as the Fourier transform of a spherical top-hat filter with smoothing length $R_s = (3M/4\pi\bar{\rho})^{1/3}$,

$$W_{R_s}(k) = \frac{3 [\sin(kR_s) - kR_s \cos(kR_s)]}{(kR_s)^3} \quad (5)$$

the general spectrum moment is

$$\sigma_{\alpha_s}^2 = \frac{1}{2\pi^2} \int_0^\infty dk k^{2(\alpha+1)} P_\Phi(k) M_{R_s}(k, z)^{-1} \quad (6)$$

2.2 Line intensity power spectrum

Here we model the [CII] line intensity power spectrum to predict how well it could constrain PNG. The relation between the mean intensity of the emission line and the luminosity of [CII]-luminous galaxies in their host halos (Visbal & Loeb 2010; Moradinezhad Dizgah & Keating 2019) at redshift z is expressed as

$$\langle I_{\text{CII}} \rangle(z) = \frac{c^2 f_{\text{duty}}}{2k_B v_{\text{obs}}^2} \int_{M_{\text{min}}}^{M_{\text{max}}} dM \frac{dn}{dM} \frac{L(M, z)}{4\pi \mathcal{D}_L^2} \left(\frac{dl}{d\theta} \right)^2 \frac{dl}{dv} \quad (7)$$

where M_{min} and M_{max} are the minimum and maximum mass of [CII]-emitting halos, f_{duty} is the duty cycle of line emitting halos, (i.e. the fraction of halos in the given mass range which emit [CII] line at redshift z), dn/dM is the halo mass function, $L(M, z)$ is the luminosity of the [CII]-luminous galaxies from dark matter halo of mass M at redshift z , \mathcal{D}_L is the luminosity distance. We set $M_{\text{min}} = 10^9 M_\odot$ and $M_{\text{max}} = 10^{14.5} M_\odot$. We replace f_{duty} with $p_{n,\sigma}$ as given in (Moradinezhad Dizgah & Keating 2019). We use the Tinker halo mass function (Tinker et al. 2008). $dl/d\theta$ and dl/dv convert comoving lengths l to frequency ν and angular size θ , $dl/d\theta = D_{\text{A,co}}(z)$, $\frac{dl}{dv} = \frac{c(1+z)}{v_{\text{obs}} H(z)}$, where $D_{\text{A,co}}(z)$ is the comoving angular diameter distance (For a flat universe, $D_{\text{A,co}}(z) = \chi(z)$ where $\chi(z)$ is the co-moving distance to redshift z) and $H(z)$ is the Hubble parameter at redshift z . For our fiducial model we use the result of the $m1$ model of Silva et al. (2015) to relate the [CII] luminosity to the average star formation rate $\overline{\text{SFR}}(M, z)$ of Behroozi et al. (2013)

$$\log L_{\text{CII}} = 0.8475 \times \log \overline{\text{SFR}}(M, z) + 7.2203 \quad (8)$$

[CII] line bias is related to halo bias $b_h(M, z)$ as (Moradinezhad Dizgah & Keating 2019)

$$b_{\text{line}}(z) = \frac{\int_{M_{\text{min}}}^{M_{\text{max}}} dM \frac{dn}{dM} b_h(M, z) L(M, z)}{\int_{M_{\text{min}}}^{M_{\text{max}}} dM \frac{dn}{dM} L(M, z)} \quad (9)$$

We use halo bias $b_h(M, z)$ of (Tinker et al. 2010).

Setting $z = 3.60$, we get $\langle I_{\text{CII}}(3.6) \rangle = 0.30 \mu\text{K}$ from (7) and $b_{\text{line}}(3.6) = 3.47$ from (9).

The shot noise power spectrum is

$$P_{\text{shot}}(z) = \frac{c^4 f_{\text{duty}}}{4k_B^2 v_{\text{obs}}^4} \int_{M_{\text{min}}}^{M_{\text{max}}} dM \frac{dn}{dM} \left[\frac{L(M, z)}{4\pi \mathcal{D}_L^2} \left(\frac{dl}{d\theta} \right)^2 \frac{dl}{dv} \right]^2 \quad (10)$$

Including redshift space distortions, the line clustering power spectrum can be expressed as

$$P(k, \mu, z) = \langle I_{\text{CII}} \rangle(z)^2 b_{\text{line}}^2(z) P_0(k, z) \times \left[1 + \mu^2 \beta(k, z) \right]^2 \exp \left(-\frac{k^2 \mu^2 \sigma_v^2}{H^2(z)} \right) \quad (11)$$

The factor of $\left[1 + \mu^2 \beta(k, z) \right]^2$ comes from the Kaiser effect (Kaiser

1987), $\beta(k, z) = f/b_{\text{line}}(z)$, where f is the logarithmic derivative of the growth factor, $\mu = k_{\parallel}/k$ is the cosine of the angle between the \mathbf{k} and the line of sight direction. The factor of $\exp \left(-\frac{k^2 \mu^2 \sigma_v^2}{H^2(z)} \right)$ is from the finger-of-god effect (Jackson 1972) with the pairwise velocity dispersion approximated as $\sigma_v^2 = (1+z)^2 \left[\frac{\sigma_{\text{FOG}}^2(z)}{2} + c^2 \sigma_z^2 \right]$, where $\sigma_{\text{FOG}}(z) = \sigma_{\text{FOG},0} \sqrt{1+z}$, $\sigma_z = 0.001(1+z)$ and $\sigma_{\text{FOG},0} = 250 \text{ km.s}^{-1}$. According to Eqs. (9), (2) and (3) will manifest as a scale-dependent correction to the b_{line} and therefore to the line power spectrum (11).

2.3 Interloper contamination

Line emission of CO interloper line at redshift z_i confuses with target [CII] line by residing at the same observed frequency ν_{obs} as the [CII] line. When we convert the observed frequency interval $\Delta\nu_{\text{obs}}$ and angular separation $\Delta\theta_{\text{obs}}$ in a data cube to co-moving coordinates to calculate the power spectrum, if we adopt the target line redshift z_t , we will end up with wrong wavenumbers (Lidz & Taylor 2016). The relation between the true wavenumbers k_{\parallel} and \mathbf{k}_{\perp} and these apparent wavenumbers \tilde{k}_{\parallel} and $\tilde{\mathbf{k}}_{\perp}$, calculated by wrongly adopting the z_t for coordinate conversion, is

$$\tilde{k}_{\parallel} = \frac{H(z_t)}{H(z_i)} \frac{1+z_i}{1+z_t} k_{\parallel} = \alpha_{\parallel} k_{\parallel} \quad (12)$$

$$\tilde{\mathbf{k}}_{\perp} = \frac{D_{\text{A,co}}(z_i)}{D_{\text{A,co}}(z_t)} \mathbf{k}_{\perp} = \alpha_{\perp} \mathbf{k}_{\perp} \quad (13)$$

where α_{\parallel} and α_{\perp} are distortion factors caused by this incorrect redshift adoption. Therefore for the multiple interloper line emission case with N interloper lines, the total power spectrum in the data cube is

$$P_{\text{tot}}(\tilde{k}_{\parallel}, \tilde{\mathbf{k}}_{\perp}) = P_t(k_{\parallel}, \mathbf{k}_{\perp}) + \sum_{j=1}^N \frac{1}{\alpha_{\parallel}(z_j) \alpha_{\perp}^2(z_j)} P_j \left(\frac{\tilde{k}_{\parallel}}{\alpha_{\parallel}}, \frac{\tilde{\mathbf{k}}_{\perp}}{\alpha_{\perp}} \right) \quad (14)$$

where z_j is the redshift of the j th interloper line. In this paper we consider up to 7 CO interloper lines, with J ranging from 4 to 10 in CO ($J \rightarrow J-1$) molecule transitioning between rotational states J and $J-1$.

For CO ($1 \rightarrow 0$), expressed in units of solar luminosity, the luminosity is

$$L_{\text{CO}(1-0)} = 4.9 \times 10^{-5} L'_{\text{CO}} \quad (15)$$

Using the fit from (Carilli & Walter 2013), CO line luminosity L'_{CO} , which is expressed in units of $\text{Kkms}^{-1} \text{pc}^2$, is related to the far-infrared luminosity L_{IR} , which is in the unit of L_{\odot} as

$$\log L_{\text{IR}} = 1.37 \times \log L'_{\text{CO}} - 1.74 \quad (16)$$

We use the base model of Li et al. (2016), where L_{IR} is related to the $\overline{\text{SFR}}$ in units of $M_{\odot} \text{yr}^{-1}$ via Kennicutt relation (Kennicutt 1998) using the results of Behroozi et al. (2013)

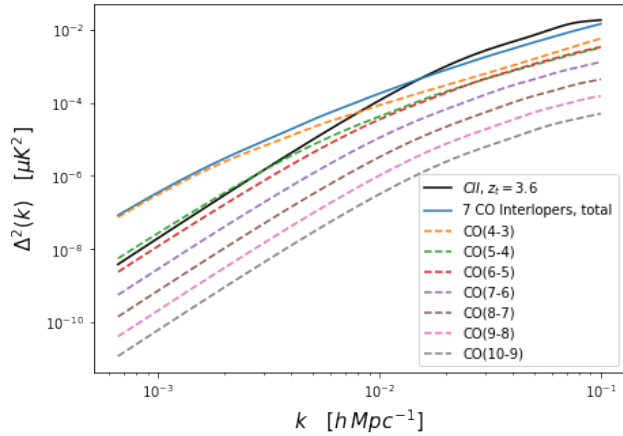
$$\overline{\text{SFR}}(M, z) = \delta_{\text{MF}} \times 10^{-10} L_{\text{IR}} \quad (17)$$

We use $\delta_{\text{MF}} = 1$ (Behroozi et al. 2013; Li et al. 2016).

Using Eq. (7) we get intensities for CO ($1 \rightarrow 0$) at different redshifts z_j that will interlope with the [CII] target line at $z = 3.6$, i.e. $\frac{J \times 115 \text{ GHz}}{z_j+1} = \frac{1901 \text{ GHz}}{3.6+1}$. In order to construct a rough estimate of the interloper luminosities, we use the ratio between the luminosity

Table 1. Redshifts z_j , intensities $\langle I \rangle$ (in units of μK) and line biases b_{line} for the 7 interloper CO lines

J	4	5	6	7	8	9	10
z_j	0.113	0.391	0.670	0.948	1.226	1.504	1.783
$\langle I \rangle$	0.07	0.08	0.10	0.06	0.04	0.03	0.02
b_{line}	0.6	0.8	1	1.2	1.3	1.4	1.6

**Figure 1.** Spherically averaged $k^3 P(k)/(2\pi)^2$. The black solid line shows the [CII] line power spectrum at $z = 3.6$. The blue solid line shows the total interloper power spectrum from the 7 CO interloper lines. The 7 dashed lines show the interloper power spectrum for the 7 CO interloper lines respectively.

of 7 CO interloper lines with J ranging from 4 to 10 and that for the CO ($1 \rightarrow 0$) (Visbal & Loeb 2010) to get the intensities for these 7 interlopers, we also calculate the line biases for these interloper lines according to Eq. (9); these values for interlopers are listed in Table 1.

According to the values in Table 1, we plot spherically averaged $k^3 P(k)/(2\pi)^2$ of the [CII] line at $z = 3.6$ and the 7 CO lines that interlope with it in Figure 1. As in previous work (Lidz & Taylor 2016; Gong et al. 2012), we plot contours of constant power in the $k_{\perp} - k_{\parallel}$ plane in Figure 2 and 3 to visualize the anisotropy of the sum of the seven interloper power spectrum. Figure 2 characterizes the redshift space distortion in the target [CII] line power spectrum. The contours in Figure 3 illustrate the anisotropy of the power spectrum summation of the interloper CO lines from the coordinate mapping distortion, with the k_{\parallel} strongly elongated.

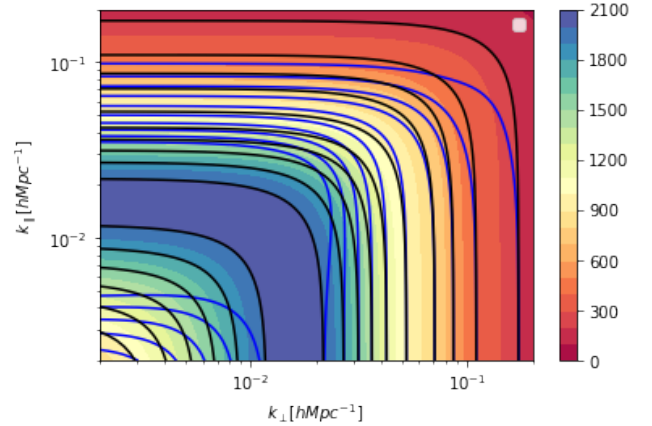
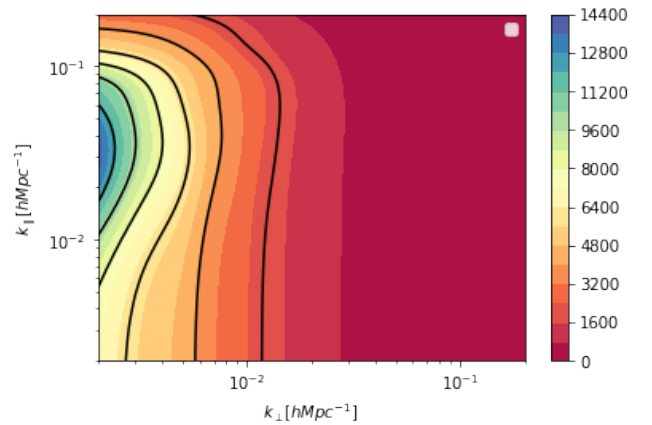
3 PARAMETER ESTIMATION FORMALISM

The first part of this section describes the Fisher matrix forecast methodology. In the second part we derive the interloper bias to the measured power spectrum.

3.1 Fisher matrix forecast

We use the Fisher matrix methodology to forecast how well a hypothetical [CII] survey will constrain f_{NL} . We first consider the simple case with only 1 CO interloper CO ($4 \rightarrow 3$). We consider a parameter space \mathbf{q} . Our forecast is conducted at $z_t = 3.6$.

We investigate whether the f_{NL} and [CII] target line, which is characterized by I_{CII} and b_{CII} can be forecasted precisely with

**Figure 2.** Contours of constant power in the $k_{\perp} - k_{\parallel}$ plane for the target [CII] power spectrum at $z_t = 3.6$. The black contours neglect redshift space distortions, while the black contours and color-scale include them. The colorbar is in units of $\mu K^2(\text{Mpc}/h)^3$ **Figure 3.** The contour with lowest power is at $P(k) = 2 \times 10^3 \mu K^2(\text{Mpc}/h)^3$ and the contours increase inwards as $\Delta P = 2 \times 10^3 \mu K^2(\text{Mpc}/h)^3$. The black contours illustrate the anisotropy of the summation of the seven interloper line power spectrum including redshift space distortion and coordinate mapping distortion. The k_{\parallel} direction is strongly elongated

the interloper contamination which is characterized by $\langle I_{\text{CO}(4 \rightarrow 3)} \rangle$ and $b_{\text{CO}(4 \rightarrow 3)}$ by calculating the Fisher matrix with component for the i th and j th of \mathbf{q}

$$F_{ij} = \int_{-1}^1 d\mu \int_{k_{\min}}^{k_{\max}} \frac{k^2 dk}{8\pi^2} V_{\text{eff}}(k, \mu, z_t) \frac{\partial \ln P_{\text{tot}}(k, \mu, z_t)}{\partial q_i} \times \frac{\partial \ln P_{\text{tot}}(k, \mu, z_t)}{\partial q_j} \quad (18)$$

where the total power spectrum including the [CII] and CO ($4 \rightarrow 3$) power is given as Eq. (14). V_{eff} is the effective volume of the redshift bin at $z_t = 3.6$, $V_{\text{eff}} = \left[\frac{P_{\text{tot}}(k, \mu, z_t)}{P_{\text{tot}}(k, \mu, z_t) + P_{\text{shot}}(z_t) + \bar{P}_N(k, \mu)} \right]^2 V_i$, $P_{\text{shot}}(z_t)$ is given as Eq. (10), $\bar{P}_N(k, \mu)$ is the effective instrumental noise power spectrum given later as Eq. (27), V_i is the volume of the redshift bin between z_{\min} and z_{\max} with a fraction of the

sky f_{sky} ; specifically, $V_i = \frac{4\pi}{3} f_{sky} [\chi^3(z_{max}) - \chi^3(z_{min})]$, where $\chi(z)$ is the co-moving distance to redshift z .

3.2 Parameter bias forecast

The bias from interloper contamination in power spectrum detection can be calculated using the formalism constructed in Pullen et al. (2016). The parameter bias is

$$\Delta \mathbf{q} = \mathbf{F}^{-1} \Delta \mathbf{D} \quad (19)$$

where \mathbf{F} is the Fisher matrix with the parameter space of \mathbf{q} . The j th component of $\Delta \mathbf{D}$ is given as

$$\begin{aligned} \Delta D_j &= \int_{-1}^1 d\mu \int_{k_{min}}^{k_{max}} \frac{k^2 dk}{8\pi^2} V_{eff}(k, \mu, z_t) \frac{\Delta P_t(k, \mu, z_t)}{P_t} \\ &\times \frac{\partial \ln P_t(k, \mu, z_t)}{\partial q_j} \end{aligned} \quad (20)$$

where $\Delta P_t(k, \mu, z_t)$ is the bias the interlopers contribute to the target power spectrum $P_t(k, \mu, z_t)$, i.e. the second term in Eq. (10).

4 FIDUCIAL SURVEY AND RESULTS

Having quantified the PNG contribution to the [CII] line power spectrum and its interloper contamination, we describe our hypothetical fiducial survey in the first part of this section, and present forecasts for using this to remove the CO interloper contributions from the [CII] local shape PNG power spectrum detection in the second part.

4.1 Fiducial survey description

As in Moradinezhad Dizgah & Keating (2019), we consider an Planck-like telescope having an aperture with dish length of $D_{ant} = 1.5$ m. We assume a frequency range of 310-620 GHz, corresponding to a [CII] redshift range of $z = 2.06 - 5.13$, and a frequency resolution $\Delta\nu = 0.4$ GHz, aperture temperature $T_{aperture} = 40$ K, and approximately $N_{det} = 10^4$ detectors working for $\tau_{tot} = 4 \times 10^4$ hours. We assume a survey sky coverage fraction $f_{sky} = 0.34$, which leads to an angular limit on the sky of $\theta_{max} = \sqrt{\Omega_{surv}} = \sqrt{4\pi f_{sky}} = 118^\circ$.

We include in our noise model photon noise from the CMB ($T_B = 2.725$ K), galactic dust ($T_B = 18$ K) and zodiacal dust ($T_B = 240$ K) contributions. The emissivity of the dust is $\varepsilon = \varepsilon_o (\nu/\nu_o)^\beta$, where for galactic dust emission $\varepsilon_o = 2 \times 10^{-4}$, $\nu_o = 3$ THz, $\beta = 2$; while for zodiacal dust emission $\varepsilon_o = 3 \times 10^{-7}$, $\nu_o = 2$ THz, $\beta = 2$. The radiation emitted at frequency ν is

$$I_\nu = \varepsilon(\nu) B_\nu(T) = \varepsilon(\nu) \frac{2h\nu^3}{c^2} \frac{1}{e^{\frac{h\nu}{k_B T_B}} - 1}. \quad (21)$$

The Rayleigh-Jeans Law yields

$$T_{dust} = \frac{\varepsilon(\nu) B_\nu(T) c^2}{2\nu^2 k_B} = \varepsilon(\nu) h\nu \frac{1}{k_B (e^{\frac{h\nu}{k_B T_B}} - 1)} \quad (22)$$

From Eq. (22) we get that at the observed frequency for the [CII] line, $T_{galactic\ dust} = 46\mu K$ and $T_{zodiacal\ dust} = 53\mu K$; therefore the systematic temperature is

$$T_{sys} = T_{aperture} + T_{CMB} + T_{zodiacal\ dust} + T_{galactic\ dust} = 42.725K \quad (23)$$

Table 2. Fisher analysis results for f_{NL}^{loc}

Interloper number	0	1	7
$\sigma(f_{NL}^{loc})$ for auto spectrum	1.32	1.64	4.04
$\sigma(f_{NL}^{loc})$ for cross-correlation	0.65	0.69	0.85

The instrumental noise for each k-mode is (Moradinezhad Dizgah et al. 2019)

$$P_N = \frac{T_{sys}^2}{\tau_{tot} N_{det}} \Omega_{surv} \left(\frac{dl}{d\theta} \right)^2 \frac{dl}{dv}. \quad (24)$$

The scale-independent correction to the clustering bias is relatively negligible at small scales, so we set $k_{max} = 0.1 h \text{ Mpc}^{-1}$.

We consider the largest scales recoverable from foreground contamination. We model this with the parameter η_{min} , defined as the ratio of the observed frequency divided by the maximum bandwidth over which the frequency dependent response of the instrument is assumed to be smooth, as in Moradinezhad Dizgah & Keating (2019). We model the recoverable largest-scale per-parallel mode from foregrounds as $k_{\parallel, min} = 2\pi\eta_{min} [\nu_{obs} dl/dv]^{-1}$. Setting $\eta_{min} = 4.5$, which is $3\times$ the frequency-bandwidth ratio of the fiducial instrument, we have $k_{\parallel, min} = 0.0077 \text{ Mpc}^{-1}$. The survey area sets the largest-scale perpendicular mode, given by $k_{\perp, min} = 2\pi [2 \sin(\theta_{max}/2) \frac{dl}{d\theta}]^{-1} = 0.0005 \text{ Mpc}^{-1}$. The smallest-scale modes are generated by the spatial and spectral resolutions respectively, $k_{\perp, max} \approx 2\pi [\frac{c/\nu_{obs}}{D_{ant}} \frac{dl}{d\theta}]^{-1}$, $k_{\parallel, max} \approx 2\pi [\delta\nu \frac{dl}{dv}]^{-1}$.

We introduce the attenuation of the signal due to foregrounds as in Moradinezhad Dizgah & Keating (2019)

$$\gamma_{min}(k_{\perp}, k_{\parallel}) = \left(1 - e^{-k_{\perp}^2/(k_{\perp, min}/2)^2}\right) \times \left(1 - e^{-k_{\parallel}^2/(k_{\parallel, min}/2)^2}\right), \quad (25)$$

and due to finite spectral and angular resolution

$$\gamma_{max}(k_{\perp}, k_{\parallel}) = e^{-(k_{\perp}^2/k_{\perp, max}^2 + k_{\parallel}^2/k_{\parallel, max}^2)}, \quad (26)$$

writing the effective instrumental noise as

$$\tilde{P}_N(k, \mu, z) = P_N \gamma_{max}^{-1}(k, \mu) \gamma_{min}^{-1}(k, \mu). \quad (27)$$

4.2 Forecast results

In this section we forecast the local shape f_{NL} measured from only the auto-power spectrum. The Fisher analysis results for this section are listed in Table 2.

In the first scenario we assume there is no interloper contamination. The parameter space includes four parameters $\mathbf{q} = \{f_{NL}^{loc}, \langle I_{CII} \rangle, b_{CII}, P_{shot}^{CII}\}$. We set the fiducial value of the parameters as $f_{NL}^{loc} = 0$, $\langle I_{CII} \rangle = 0.30\mu K$, $b_{CII} = 3.47$, as what was calculated before, $P_{shot}^{CII} = 13.57\mu K^2 (\text{Mpc}/h)^3$. We find $\sigma(f_{NL}^{loc}) = 1.32$, which being of order $\mathcal{O}(1)$ is the target level of uncertainty needed to discriminate between inflation models. This result deviates from the one from Moradinezhad Dizgah & Keating (2019) because we adopted different fiducial survey parameters, and therefore yield a smaller instrumental noise. We plot the $1 - \sigma$ errors in different parameter planes shown as the yellow ellipses in Figure (4).

In the second scenario we include a contamination from one interloper CO (4 \rightarrow 3) at $z_j = 0.113$ according to the second term in Eq. (14), the anisotropic contribution to the [CII] power spectrum due to CO (4 \rightarrow 3).

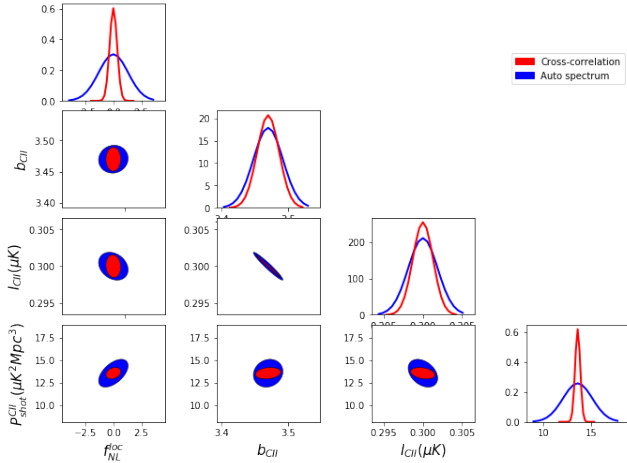


Figure 4. $1 - \sigma$ forecast of the constraint on f_{NL}^{loc} for the Fisher analysis without considering interlopers.

The parameter space now includes seven parameters $\mathbf{q} = \{f_{NL}^{loc}, \langle I_{CII} \rangle, b_{CII}, \langle I_{CO(4 \rightarrow 3)}(z_j) \rangle, b_{CO(4 \rightarrow 3)}(z_j), P_{shot}^{CII}, P_{shot}^{CO(4 \rightarrow 3)}(z_j)\}$. We set the fiducial values of the interloper parameters as $\langle I_{CO(4 \rightarrow 3)}(z_j) \rangle = 0.07 \mu K$, $b_{CO(4 \rightarrow 3)}(z_j) = 0.6$ as listed in Table 1, $P_{shot}^{CO(4 \rightarrow 3)}(z_j) = 1.35 \mu K^2 (\text{Mpc}/h)^3$, and the remaining parameters are set as in the first scenario. We compute the marginalized $\sigma(f_{NL}^{loc}) = 1.64$, a 24% increase due to interloper contamination. We plot the $1 - \sigma$ errors in different parameter planes shown as yellow ellipses in Figure (5). Alternatively, if we consider the interloper contamination as pure noise other than mixing signals for the target CII line, the parameter space becomes $\mathbf{q} = \{f_{NL}^{loc}, \langle I_{CII} \rangle, b_{CII}, P_{shot}^{CII}\}$ and we find $\sigma(f_{NL}^{loc}) = 1.60$. Note that treating the CO(4-3) line as noise gives you slightly less error in f_{NL}^{loc} because this model has less degrees of freedom. The uncertainty in f_{NL}^{loc} becomes much larger when multiple interloper lines are introduced. If we include interloper contamination from all the 7 CO interlopers whose fiducial intensities and biases are given in Table 1 and marginalize over all these fiducial quantities, we get $\sigma(f_{NL}^{loc}) = 4.04$.

Considering the case where one interloper $P_{CO(4 \rightarrow 3)}$ biases the measured power spectrum, we get the parameter bias $\Delta \mathbf{p}^T = [\Delta f_{NL}^{loc}, \Delta b_{CII}, \Delta \langle I_{CII} \rangle, \Delta P_{shot}^{CII}] = [4.54, -5.45, 0.49, 6.87]$. This would suggest one interloper can masquerade as a 2.8σ detection of f_{NL} while providing a false positive for non-standard inflation models. This result shows that the presence of interlopers are prohibitive when attempting to measure f_{NL}^{loc} using an auto-power spectrum.

5 CROSS-CORRELATION WITH OTHER LINES

According to our Fisher analysis results, interloper contamination highly biases local PNG constraints. Next, we consider cross-correlating the target [CII] line with a data cube centered on a different frequency corresponding to a target redshift $z_t = 3.6$ for the CO(4 → 3) line, which could reduce the interloper contamination to the PNG constraint. We label the auto power spectra of the [CII] and CO(4 → 3) at $z_t = 3.6$ as $P_{CII}(k, \mu)$ and $P_{CO(4 \rightarrow 3)}(k, \mu)$, respectively. The cross-power spectrum between

the [CII] and CO(4 → 3) data cubes is

$$P_x(k, \mu) = I_{CII} I_{CO(4 \rightarrow 3)} b_{CII} b_{CO(4 \rightarrow 3)} \left(1 + \beta_{CII} \mu^2\right) \times \left(1 + \beta_{CO(4 \rightarrow 3)} \mu^2\right) \exp\left(-\frac{k^2 \mu^2 \sigma_v^2}{H^2(z)}\right) P_0(k, z_t) + P_{shot}^X \quad (28)$$

The shot noise in the cross-power spectrum is

$$P_{shot}^X(z) = \frac{c^4 f_{duty}}{4k_B^2 v_{obsCII}^2 v_{obsCO(4 \rightarrow 3)}^2} \int_{M_{min}}^{M_{max}} dM \frac{dn}{dM} \times \left[\frac{L(M, z)}{4\pi \mathcal{D}_L^2} \left(\frac{dl}{d\theta}\right)^2 \frac{dl}{dv} \right]_{CII} \left[\frac{L(M, z)}{4\pi \mathcal{D}_L^2} \left(\frac{dl}{d\theta}\right)^2 \frac{dl}{dv} \right]_{CO(4 \rightarrow 3)} \quad (29)$$

Let the observables be the data vector $\mathbf{d} = \{P_{CII}(k, \mu), P_{CO(4 \rightarrow 3)}(k, \mu), P_x\}$. We consider a parameter space \mathbf{q} at $z_t = 3.6$. The Fisher matrix element with component for the i th and j th of \mathbf{q} is (Tegmark et al. 1997)

$$F_{ij} = V_i \int_{-1}^1 d\mu \int_{k_{min}}^{k_{max}} \frac{k^2 dk}{8\pi^2} \frac{\partial \mathbf{d}}{\partial q_i} \Xi^{-1} \frac{\partial \mathbf{d}^T}{\partial q_j} \quad (30)$$

where the entries of the covariance matrix Ξ are given in Lidz et al. (2009). We can also use Eq. 19 to compute the shift in the parameters due to interloper contamination. In this case, the formula for ΔD becomes

$$\Delta D_j = V_j \int_{-1}^1 d\mu \int_{k_{min}}^{k_{max}} \frac{k^2 dk}{8\pi^2} \Delta \mathbf{d} \Xi^{-1} \frac{\partial \mathbf{d}^T}{\partial q_j}, \quad (31)$$

where $\Delta \mathbf{d}$ is the shift in the data vector due to interloper contamination.

The Fisher analysis results for this section are listed in Table 2.

We first consider the scenario without interloper lines, i.e. only the first term in Eq. 14 is considered. The parameter space is $\mathbf{q} = \{f_{NL}^{loc}, \langle I_{CII}(z_t) \rangle, b_{CII}(z_t), P_{shot}^{CII}(z_t), \langle I_{CO(4 \rightarrow 3)}(z_t) \rangle, b_{CO(4 \rightarrow 3)}(z_t), P_{shot}^{CO(4 \rightarrow 3)}(z_t), P_{shot}^X\}$, in which the fiducial values for the f_{NL}^{loc} , $\langle I_{CII}(z_t) \rangle$, $b_{CII}(z_t)$ are set as in in Section 4, $\langle I_{CO(4 \rightarrow 3)}(z_t) \rangle$ and $b_{CO(4 \rightarrow 3)}(z_t)$ are calculated from the method discussed in Section 2, $\langle I_{CO(4 \rightarrow 3)}(z_t) \rangle = 0.60 \mu K$, $b_{CO(4 \rightarrow 3)}(z_t) = 2.8$, $P_{shot}^{CO(4 \rightarrow 3)}(z_t) = 88.01 \mu K^2 (\text{Mpc}/h)^3$, $P_{shot}^X = 32.13 \mu K^2 (\text{Mpc}/h)^3$. We use the 8×8 Fisher matrix from Eq. 30 to find the constraint on the parameters. $1 - \sigma$ errors in different parameter planes are shown as the yellow ellipses in Figure 4. In this Fisher analysis assuming the dataset $\{P_{CII}(k, \mu), P_{CO(4 \rightarrow 3)}(k, \mu), P_x\}$, we find $\sigma(f_{NL}^{loc}) = 0.65$, much lower than the initial experimental setup value for the [CII] auto power spectrum of $\sigma(f_{NL}^{loc}) = 1.32$. This result is expected since having multiple lines add more constraining power, and we benefit from the multi-tracer cosmic variance cancellation, as addressed in Liu & Breyse (2021).

In the second scenario we include the contamination from one interloper CO(4 → 3) at redshift 0.113 according to the second term in Eq. 14, the anisotropic contribution to the [CII] power spectrum due to CO(4 → 3).

The parameter space includes eleven parameters $\mathbf{q} = \{f_{NL}^{loc}, \langle I_{CII}(z_t) \rangle, b_{CII}(z_t), P_{shot}^{CII}(z_t), \langle I_{CO(4 \rightarrow 3)}(z_t) \rangle, b_{CO(4 \rightarrow 3)}(z_t), P_{shot}^{CO(4 \rightarrow 3)}(z_t), \langle I_{intCO(4 \rightarrow 3)}(z_j) \rangle, b_{intCO(4 \rightarrow 3)}(z_j), P_{shot}^{CO(4 \rightarrow 3)}(z_j), P_{shot}^X\}$, in which the fiducial values $\langle I_{intCO(4 \rightarrow 3)}(z_j) \rangle$ and $b_{intCO(4 \rightarrow 3)}(z_j)$ for the interloper parameters are set as section 4.2. We use the 11×11 Fisher

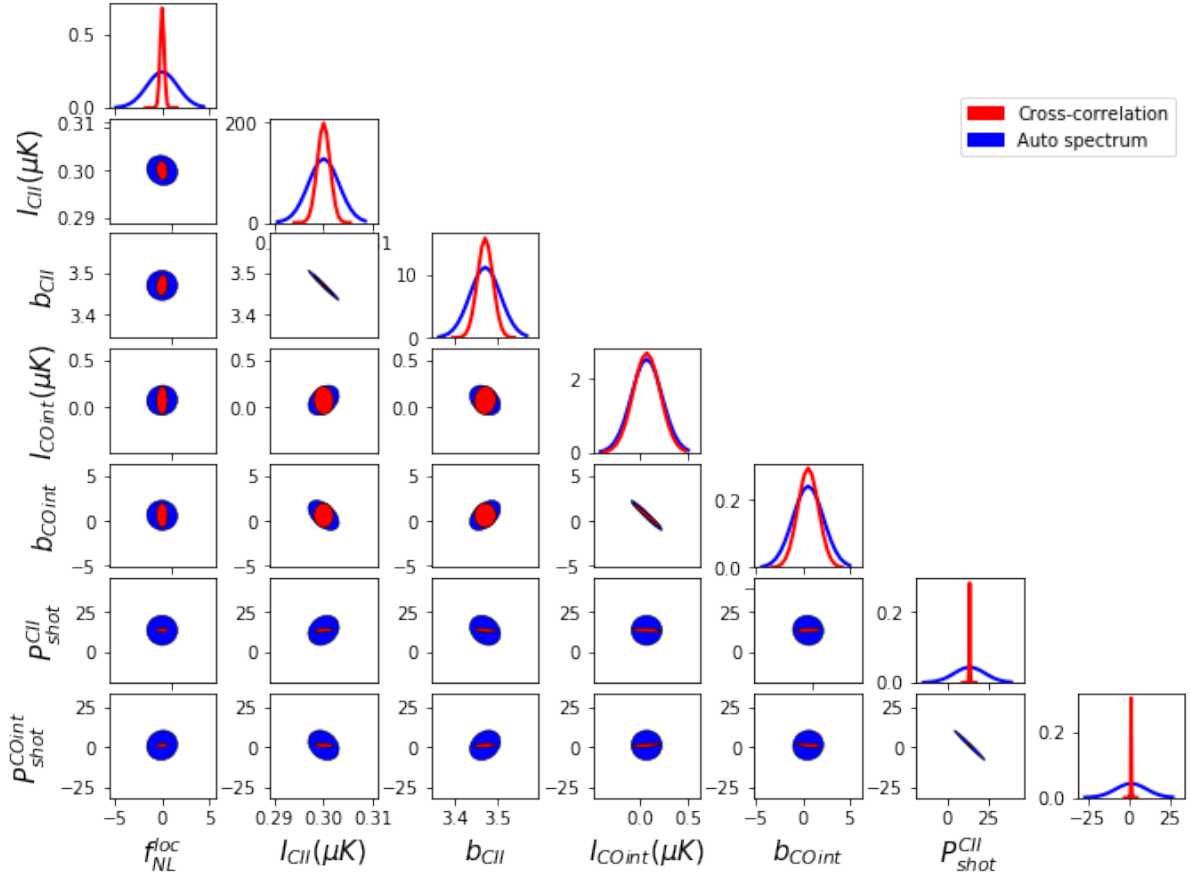


Figure 5. $1 - \sigma$ forecast of the constraint on f_{NL}^{loc} for the Fisher analysis with considering CO (4 \rightarrow 3) interloper.

matrix from Eq. 30 to find the constraint on the parameters. $1 - \sigma$ errors in different parameter planes are shown as the red ellipses in Figure 5. We find that in this Fisher analysis $\sigma(f_{NL}^{loc}) = 0.69$, which is only 6% more than the predicted f_{NL} error in the case with no interlopers. Note this increase is 4x less than the increase in the f_{NL} error from the auto-power spectrum constraint. We also see that the error for the two cross-correlation cases, one with no interlopers and one with interlopers, are equal within less than 6%, suggesting that interlopers do not significantly bias measurements of f_{NL} when the auto and cross-power spectra are used jointly. Alternatively, if we consider the interloper contamination as pure noise other than mixing signals for the target CII line, we find $\sigma(f_{NL}^{loc}) = 0.78$, the parameter bias $\Delta \mathbf{p}^T = \Delta[f_{NL}^{loc}, \langle I_{CII}(z_t) \rangle, b_{CII}(z_t), \langle I_{CO(4 \rightarrow 3)}(z_t) \rangle, b_{CO(4 \rightarrow 3)}(z_t), P_{shot}^{CII}(z_t), P_{shot}^{CO(4 \rightarrow 3)}(z_t)] = [3.29, 0.21, -2.29, -0.037, 0.15, 6.77, 30.89]$. This result shows that including the interlopers as pure noise other than signals can not help to remove the interloper contamination. If we assume the dataset only includes the cross-spectrum $\{P_x\}$, we find $\sigma(f_{NL}^{loc}) = 0.85$, slightly higher than that from doing the cross-correlation considering auto-spectrum. This result shows that including the auto-spectrum does not aid much when removing the interlopers if you treat it as noise.

If we include all the 7 interlopers CO (4 \rightarrow 3) to CO (10 \rightarrow 9) at lower redshift, with all their intensities and biases being added to the parameter space \mathbf{q} , in the cross-correlated Fisher analysis

Table 3. Fisher analysis results for f_{NL}^{orth}

Interloper number	0	1
$\sigma(f_{NL}^{orth})$ for auto spectrum	52.75	7.15
$\sigma(f_{NL}^{orth})$ for cross-correlation	42.24	7.05

we get $\sigma(f_{NL}^{loc}) = 0.85$, dropping significantly as compared to $\sigma(f_{NL}^{loc}) = 4.04$ for the [CII] auto power spectrum Fisher analysis.

6 CONSTRAINTS ON ORTHOGONAL SHAPE PNG

In this section we derive how interlopers affect constraints on measurements of orthogonal shape PNG. We present the forecasts for the removal of CO interloper contributions to the [CII] auto power spectrum detection in the first subsection. In the second subsection we present the Fisher forecasts for the cross-correlation between [CII] line and other lines at the same redshift. The Fisher analysis results for this section are listed in Table 3.

6.1 Auto power spectrum Fisher forecast

We forecast the orthogonal shape PNG rather than the equilateral PNG since the former brings larger correction to the clustering bias, and thus a stronger constraint on f_{NL} . We set the fiducial

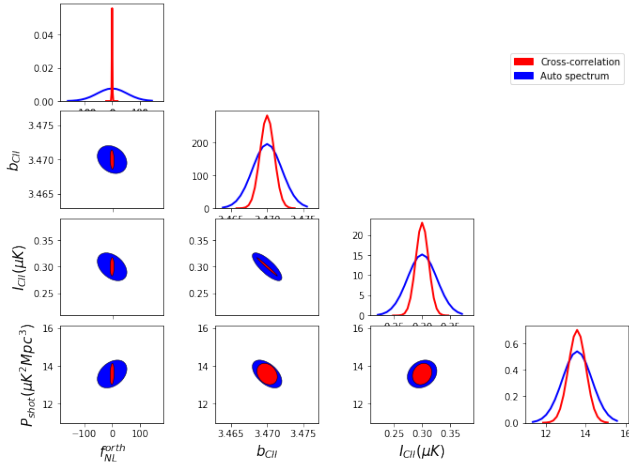


Figure 6. $1 - \sigma$ forecast of the constraint on f_{NL}^{orth} for the Fisher analysis without considering interlopers.

value $f_{NL}^{orth} = 0$. We adopt the same fiducial survey and remaining parameter values as described in Section 4.

In the first scenario we assume there is no interloper contamination. The parameter space includes three parameters $\mathbf{q} = \{f_{NL}^{orth}, \langle I_{CII} \rangle, b_{CII}, P_{shot}^{CII}\}$. We find $\sigma(f_{NL}^{orth}) = 52.75$, and we plot the $1 - \sigma$ errors in different parameter planes shown as yellow ellipses in Figure 6.

In the second scenario we include the interloper contamination from one interloper CO(4 → 3) at $z_j = 0.113$. The parameter space contains five parameters $\mathbf{q} = \{f_{NL}^{orth}, \langle I_{CII}(z_t) \rangle, b_{CII}(z_t), P_{shot}^{CII}(z_t), \langle I_{CO(4 \rightarrow 3)}(z_j) \rangle, b_{CO(4 \rightarrow 3)}(z_j), P_{shot}^{CO(4 \rightarrow 3)}(z_j)\}$. We plot the $1 - \sigma$ errors in different parameter planes shown as yellow ellipses in Figure 7. We find the marginalized $\sigma(f_{NL}^{orth}) = 42.24$. The reason for this error being smaller than that in the first scenario, as contrary to the case for f_{NL}^{loc} is that Δb_h^{orth} in (4) are of the same sign for the target line and the interloper, while Δb_h^{loc} in (3) are of different signs.

Considering the case where one interloper $P_{CO(4 \rightarrow 3)}$ biases the measured power spectrum, we compute the parameter bias $\Delta \mathbf{p}^T = [\Delta f_{NL}^{orth}, \Delta b_{CII}, \Delta \langle I_{CII} \rangle, \Delta P_{shot}^{CII}] = [49.20, -5.58, 0.51, 6.25]$. This points to a modest bias relative to the predicted errors, in that the interlopers could masquerade as a 1.2-sigma measurement of f_{NL} .

6.2 Cross-correlation Fisher forecast

We adopt the same fiducial survey and value of parameters for cross-correlation as in Section 5. We first consider the scenario without interloper lines with the parameter space being $\mathbf{q} = \{f_{NL}^{orth}, \langle I_{CII}(z_t) \rangle, b_{CII}(z_t), P_{shot}^{CII}(z_t), \langle I_{CO(4 \rightarrow 3)}(z_t) \rangle, b_{CO(4 \rightarrow 3)}(z_t), P_{shot}^{CO(4 \rightarrow 3)}(z_t), P_{shot}^X\}$. $1 - \sigma$ errors in different parameter planes are shown as red ellipses in Figure 6. We find that in this cross-correlated Fisher analysis $\sigma(f_{NL}^{orth}) = 7.05$, dropping significantly as compared to $\sigma(f_{NL}^{orth}) = 52.75$ for the [CII] auto power spectrum Fisher analysis.

In the second scenario we include the interloper contamination from one interloper CO(4 → 3) at redshift 0.113. The parameter space includes seven parameters $\mathbf{q} = \{f_{NL}^{orth}, \langle I_{CII}(z_t) \rangle, b_{CII}(z_t), P_{shot}^{CII}(z_t), \langle I_{CO(4 \rightarrow 3)}(z_t) \rangle,$

$b_{CO(4 \rightarrow 3)}(z_t), P_{shot}^{CO(4 \rightarrow 3)}(z_t), \langle I_{int CO(4 \rightarrow 3)}(z_j) \rangle, b_{int CO(4 \rightarrow 3)}(z_j), P_{shot}^{CO(4 \rightarrow 3)}(z_j), P_{shot}^X\}$. $1 - \sigma$ errors in different parameter planes are shown as red ellipses in Figure 7. We note that in this cross-correlated Fisher analysis $\sigma(f_{NL}^{orth}) = 7.05$, dropping significantly as compared to $\sigma(f_{NL}^{orth}) = 42.24$ for the [CII] auto power spectrum Fisher analysis. Similar to the local PNG case, cross-power spectra tend to remove the effect of interlopers when measuring f_{NL} . Alternatively, if we consider the interloper contamination as pure noise other than mixing signals for the target CII line, we find $\sigma(f_{NL}^{orth}) = 7.29$, the parameter bias $\Delta \mathbf{p}^T = [f_{NL}^{orth}, \langle I_{CII}(z_t) \rangle, b_{CII}(z_t), \langle I_{CO(4 \rightarrow 3)}(z_t) \rangle, b_{CO(4 \rightarrow 3)}(z_t), P_{shot}^{CII}(z_t), P_{shot}^{CO}(z_t)] = [59.31, 0.47, -5.53, 0.041, -0.20, 6.56, 30.84]$. This results shows that including the interlopers as pure noise other than signals can not help to remove the interloper contamination. If we assume the dataset only includes the cross-spectrum $\{P_x\}$, we find $\sigma(f_{NL}^{orth}) = 13.51$, larger than that from considering both the cross-spectrum and the auto-spectra. This result shows that including the auto-spectrum is necessary for removing the interlopers when treating it as noise.

7 DISCUSSION

In this section we discuss how the PNG constraints depend on astrophysical models. Specifically, we consider how both different modelling of CO line luminosity and the minimum mass of halos that emit lines affect the PNG constraints.

We set $M_{min} = 10^9 M_\odot$ in our base model. In the fiducial [CII] model we use throughout the paper, we set the minimum halo mass for [CII] line emission to be $M_{min} = 10^9 M_\odot$. This parameter is very uncertain, with reasonable values between $M_{min} = 10^9 - 10^{11} M_\odot$. We find when setting $M_{min} = 10^{10} M_\odot$ without considering interloper contamination, $\langle I_{CII}(z_t) \rangle$ gets lower and therefore yields a weaker constraint. Specifically, for the case with only the auto-power spectrum only and no interlopers present, $\sigma(f_{NL}^{loc}) = 1.54$, a 17% increase. For the case with both auto-power and cross-power spectrum, $\sigma(f_{NL}^{loc}) = 0.78$, a 13% increase.

For the fiducial CO model in this work we use the Li et al. (2016) model for the interlopers. Including only one CO interloper CO(4 → 3) line contamination, we consider two other models with the CO luminosity linearly related to the halo mass. In model A considering $f_{duty} = t_s / t_{age}(z)$ in Pullen et al. (2013), we find a lower intensity for CO(4 → 3), and thus a stronger constraint on PNG. Specifically, for the auto-power only case with one interloper we find $\sigma(f_{NL}^{loc}) = 1.55$, a 6% reduction; for the case with both auto-power and cross-power, $\sigma(f_{NL}^{loc}) = 0.67$, a 3% reduction. In Keating et al. (2016), we get higher intensity for CO(4 → 3), and thus a weaker constraint on PNG with $\sigma(f_{NL}^{loc}) = 1.76$ and $\sigma(f_{NL}^{loc}) = 0.83$ for cases with only auto-power and with both auto-power and cross-power spectrum respectively.

We use the luminosity model in Visbal & Loeb (2010) to get the intensity ratios between CO($J \rightarrow J - 1$) and CO($1 \rightarrow 0$). Considering instead the relationship CO($J \rightarrow J - 1$) = J^3 CO($1 \rightarrow 0$) in Obreschkow et al. (2009) and get higher interloper intensities, and thus a weaker constraint on PNG with $\sigma(f_{NL}^{loc}) = 4.80$ if we include seven interlopers. While the relationship of CO($J \rightarrow J - 1$) = CO($1 \rightarrow 0$) in Lidz et al. (2011) yields lower interloper intensities, and thus a stronger constraint on PNG with $\sigma(f_{NL}^{loc}) = 1.34$ and $\sigma(f_{NL}^{loc}) = 0.60$ for cases with only auto-power and with both auto-power and cross-power spectrum respectively.

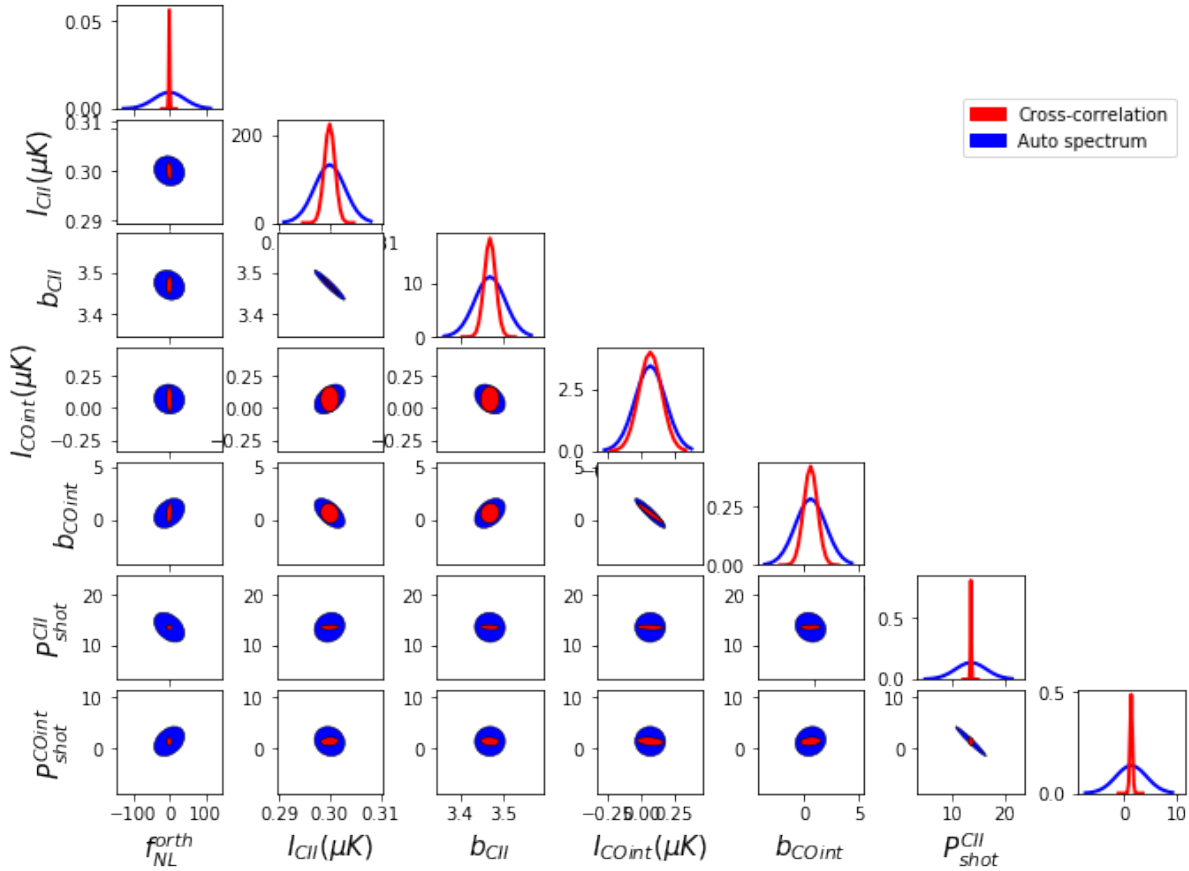


Figure 7. $1 - \sigma$ forecast of the constraint on f_{NL}^{orth} for the Fisher analysis with considering CO (4 \rightarrow 3) interloper.

8 CONCLUSION

Probing constraints on Primordial Non-Gaussianity (PNG) characterized by f_{NL} is a strong discriminant among cosmological models. PNG leads to a scale-dependent clustering bias for emission lines. We consider [CII] line intensity mapping at the target redshift $z_t = 3.6$ to model how interlopers affect measurements of f_{NL}^{loc} and f_{NL}^{orth} .

Interloper contamination from CO line confusion provides an important systematic concern for our intensity mapping method. We separate the anisotropic CO interloper contamination at the power spectrum level. We obtained constraints on f_{NL} from a future survey with and without CO lines interloping, and found that the interloper contamination leads to weaker constraints on f_{NL} along with significant bias to the parameter.

We model the cross-correlation between [CII] and CO(4-3) at the same redshift as a way to reduce the interloper contamination at target redshift. We model constraints on f_{NL} by calculating auto power spectrum and cross power spectrum between the data cubes which contain [CII] and CO(4-3). We find the interloper contamination for the PNG probing can be largely removed using this method.

Primordial Non-Gaussianity will shed light on physics of primordial fluctuations. Line intensity mapping is a potential technique to probe PNG by providing complementary information undetectable with other traditional galaxy surveys. Interloper contamination is an important systematic concern for this technique, as

obtained by using the power anisotropy separation method; but it can be reduced largely by using cross-correlation techniques.

ACKNOWLEDGEMENTS

We thank Patrick Breyse for his helpful feedback on an earlier version of this manuscript. ARP was supported by the Simons Foundation and by NASA under award numbers 80NSSC18K1014 and NNH17ZDA001N.

REFERENCES

- Abbott T. M. C., et al., 2018, *Phys. Rev. D*, **98**, 043526
- Afshordi N., Tolley A. J., 2008, *Phys. Rev. D*, **78**, 123507
- Alam S., et al., 2017, *MNRAS*, **470**, 2617
- Amendola L., et al., 2018, *Living Reviews in Relativity*, **21**, 2
- Behroozi P. S., Wechsler R. H., Conroy C., 2013, *ApJ*, **762**, L31
- Carilli C. L., Walter F., 2013, *ARA&A*, **51**, 105
- Castorina E., et al., 2019, *J. Cosmology Astropart. Phys.*, **2019**, 010
- Dai J.-P., Xia J.-Q., 2020, *MNRAS*, **491**, L61
- Dalal N., Doré O., Huterer D., Shirokov A., 2008, *Phys. Rev. D*, **77**, 123514
- Desjacques V., Jeong D., Schmidt F., 2011, *Phys. Rev. D*, **84**, 063512
- Gangui A., Lucchin F., Matarrese S., Mollerach S., 1994, *ApJ*, **430**, 447
- Gong Y., Cooray A., Silva M., Santos M. G., Bock J., Bradford C. M., Zemcov M., 2012, *ApJ*, **745**, 49
- Gong Y., Silva M., Cooray A., Santos M. G., 2014, *ApJ*, **785**, 72
- Gong Y., Chen X., Cooray A., 2020, *ApJ*, **894**, 152

- Guth A. H., 1981, *Phys. Rev. D*, **23**, 347
- Ho S., et al., 2015, *J. Cosmology Astropart. Phys.*, 2015, 040
- Jackson J. C., 1972, *MNRAS*, **156**, 1P
- Kaiser N., 1987, *MNRAS*, **227**, 1
- Keating G. K., Marrone D. P., Bower G. C., Leitch E., Carlstrom J. E., DeBoer D. R., 2016, *ApJ*, **830**, 34
- Kennicutt Robert C. J., 1998, *ARA&A*, **36**, 189
- Komatsu E., Spergel D. N., 2001, *Phys. Rev. D*, **63**, 063002
- Kovetz E., et al., 2019, *BAAS*, **51**, 101
- Leistedt B., Peiris H. V., Roth N., 2014, *Phys. Rev. Lett.*, **113**, 221301
- Li T. Y., Wechsler R. H., Devaraj K., Church S. E., 2016, *ApJ*, **817**, 169
- Lidz A., Taylor J., 2016, *ApJ*, **825**, 143
- Lidz A., Zahn O., Furlanetto S. R., McQuinn M., Hernquist L., Zaldarriaga M., 2009, *ApJ*, **690**, 252
- Lidz A., Furlanetto S. R., Oh S. P., Aguirre J., Chang T.-C., Doré O., Pritchard J. R., 2011, *ApJ*, **741**, 70
- Linde A. D., 1987, A New Inflationary Universe Scenario: A Possible Solution of the Horizon, Flatness, Homogeneity, Isotropy and Primordial Monopole Problems. p. 149
- Linde A., Mukhanov V., 1997, *Phys. Rev. D*, **56**, R535
- Liu R. H., Breysse P. C., 2021, *Phys. Rev. D*, **103**, 063520
- Lyth D. H., Ungarelli C., Wands D., 2003, *Phys. Rev. D*, **67**, 023503
- Maldacena J., 2003, *Journal of High Energy Physics*, 2003, 013
- Matarrese S., Verde L., 2008, *ApJ*, **677**, L77
- Moradinezhad Dizgah A., Keating G. K., 2019, *ApJ*, **872**, 126
- Moradinezhad Dizgah A., Keating G. K., Fialkov A., 2019, *ApJ*, **870**, L4
- Obreschkow D., Heywood I., Klöckner H. R., Rawlings S., 2009, *ApJ*, **702**, 1321
- Planck Collaboration et al., 2019, arXiv e-prints, p. arXiv:1905.05697
- Pullen A. R., Chang T.-C., Doré O., Lidz A., 2013, *ApJ*, **768**, 15
- Pullen A. R., Hirata C. M., Doré O., Raccanelli A., 2016, *PASJ*, **68**, 12
- Robertson B. E., Ellis R. S., Furlanetto S. R., Dunlop J. S., 2015, *ApJ*, **802**, L19
- Senatore L., Smith K. M., Zaldarriaga M., 2010, *J. Cosmology Astropart. Phys.*, 2010, 028
- Silva M., Santos M. G., Cooray A., Gong Y., 2015, *ApJ*, **806**, 209
- Slosar A., Hirata C., Seljak U., Ho S., Padmanabhan N., 2008, *J. Cosmology Astropart. Phys.*, 2008, 031
- Tegmark M., Taylor A., Heavens A., 1997, *Astrophys. J.*, **480**, 22
- Tinker J., Kravtsov A. V., Klypin A., Abazajian K., Warren M., Yepes G., Gottlöber S., Holz D. E., 2008, *ApJ*, **688**, 709
- Tinker J. L., Robertson B. E., Kravtsov A. V., Klypin A., Warren M. S., Yepes G., Gottlöber S., 2010, *ApJ*, **724**, 878
- Visbal E., Loeb A., 2010, *J. Cosmology Astropart. Phys.*, 2010, 016

This paper has been typeset from a $\text{\TeX}/\text{\LaTeX}$ file prepared by the author.